Available online at www.sciencedirect.com

ScienceDirect

Acta Materialia 86 (2015) 34–42

Acta MATERIALIA

www.elsevier.com/locate/actamat

Dynamic strain aging studied at the atomic scale

H. Aboulfadl, J. Deges, P. Choi and D. Raabe*

Max-Planck Institut für Eisenforschung GmbH, Department for Microstructure Physics and Alloy Design, Max-Planck-Str. 1, 40237 Düsseldorf, Germany

Received 9 October 2014; revised 14 November 2014; accepted 9 December 2014

Abstract—Dynamic strain aging arises from the interaction between solute atoms and matrix dislocations in strained metallic alloy. It initiates jerky dislocation motion and abrupt softening, causing negative strain rate sensitivity. This effect leads to instable flow phenomena at the macroscopic scale, appearing as a serrated stress–strain response and deformation banding. These macroscopic features are referred to as the Portevin–Le Chatelier effect (PLC). Here we study the atomistic origin of dynamic strain aging in an Al-4.8 at.% Mg alloy using atom probe tomography (APT) and transmission electron microscopy (TEM). Samples were prepared from as-cold rolled (90% thickness reduction), stabilized (120 °C, 20 h) and recrystallized sheets (400 °C, 10 min), respectively. In the stabilized state, Mg was found to decorate <1 1 0> aligned dislocations with up to ~12.5 at.%. Tensile tests in combination with thermographic and laser speckle observations were used to map the deformation bands for the site-specific extraction of APT samples from regions inside the PLC bands. We observed an asymmetrical Mg distribution along some of the dislocations, matching model predictions for high dislocation speeds at peak drag stress by Zhang and Curtin. In this case, the Mg distribution is characterized by depletion in the compressive regime above the dislocation slip plane and enrichment in the dilatation region below the slip plane. Mg also depletes in a tail-like form behind fast-moving dislocations, further promoting slip localization.

Keywords: Portevin–Le Chatelier effect; Atom probe tomography; Dynamic strain aging

1. Introduction

5xxx series Al–Mg alloys are widely used for automotive sheet-forming applications, where Mg is the main alloying element [1,2]. These alloys are mostly strengthened by solid-solution hardening since the Al_3Mg_2 (β phase) precipitates, formed above 5 wt.% Mg content, have no significant particle strengthening effect [1]. Upon deformation at room temperature, 5xxx Al alloys exhibit undesirable deformation traces on the as-formed sheet surface, which reduce the ductility of the material, create undesired optical effects and limit sheet-forming applications. The surface traces result from unstable plastic flow, entailing strain localization effects. Such phenomena become apparent upon straining as localized bands on the surface of tensile specimens and as serrations in stress–strain curves, known as the Portevin–Le Chatelier (PLC) effect [2–7].

The PLC effect is the macroscopic flow pattern that is associated with the phenomenon of dynamic strain aging (DSA), which occurs as a flow instability in a deforming alloy under specific conditions, such as the presence of solutes, medium strain rate and elevated temperatures, depending on the activation barriers for reorganization and the interaction between the solutes and the dislocations [6,7]. Several models have been suggested to explain DSA; however, the underlying atomistic interaction mechanisms between solutes and dislocations are still under debate [2–12]. All models agree on attributing the jerky dislocation motion and the resulting serrated flow pattern to a dynamical solute atom–dislocation interaction (SADI). In this perception, dislocation motion is assumed to be hindered by solute atoms that segregate to them. The dislocations are then assumed to be collectively released at a slightly higher resolved shear stress, resulting in negative stress/strain sensitivity, leading to flow instability, i.e. the PLC effect [5,13]. The understanding of DSA phenomena has improved over the years due to the introduction of advanced models that are based on considering SADI mechanisms at a more atomistic scale, also enabling the interpretation of temperature and strain rate effects [8,11]. Associated models dealing with the solute-drag effect have been developed [14–18], which also consider the spatial distribution of the solute atoms around mobile dislocations during deformation as a function of the dislocation velocity. Most of these models include specific assumptions about the distribution of the solutes around dislocations, and this motivated us to conduct a corresponding experimental analysis at the atomic scale. Among the various characterization techniques, atom probe tomography (APT) is one of the most suitable tools with which to analyze solute atom distributions in three dimensions with

* Corresponding author; e-mail: raabe@mpie.de

http://dx.doi.org/10.1016/j.actamat.2014.12.028
1359-6462/

near-atomic resolution [19–28]. In some cases, the resolution of APT is even high enough to resolve lattice planes in crystalline samples, enabling identification of single dislocations under certain circumstances [21–25,29–31]. This method is referred to as atom probe crystallography [29–31]. Alternatively, APT coupled with transmission electron microscopy (TEM) can help to retrieve both structural and chemical information at comparable resolutions [32–35].

In the case of atom probe crystallography, the first task required for identifying dislocation vectors in atom probe data sets lies in revealing the sample's crystallography in the 3-D reconstruction [29–31]. Several methods have been suggested for the extraction of crystallographic information from atom probe data sets [22–24]. The centers of crystallographic poles are generally observed as low atomic density zones in the detector histogram and in the associated APT reconstruction. The crystallographic orientations can be determined by identifying at least two crystallographic poles in the reconstruction. The indices of each pole are then obtained by measuring their angular distances and lattice spacings [21]. For the current work, we implemented the method suggested by Moody et al. [25], which optimizes the use of the spatial distribution map technique suggested by Geiser et al. [23]. This method enables a full crystallographic analysis through the identification of multiple crystallographic directions within a single APT reconstruction.

Dislocations can be then detected in the so crystallographically characterized APT data set via two approaches, namely either by solute segregation, as discussed by Miller [26], or by the disturbance of lattice planes due to atomic displacements in the vicinity of the dislocation core, as presented by Blavette et al. [27].

Here, we study SADI in an Al–Mg alloy using the APT technique in conjunction with crystallographic reconstruction. Site-specific sample preparation is carried out from regions inside the PLC bands formed during the tensile tests. Atom probe analyses of deformed and undeformed samples are carried out and compared with each other. TEM is also used to study the underlying dislocation configurations.

2. Experimental procedure

An aluminum alloy with 4.8 at.% Mg content was cast using vacuum induction melting. The alloy was heated at 400 °C for 3 h to ensure homogenization, then cold-rolled to 90% engineering reduction, i.e. 1 mm thickness. The sheet was cut into three samples. The first one was heat treated at 120 °C for 20 h (stabilization annealing, referred to as H36 condition [1]). During this heat treatment dislocations align into low energy configurations forming a dislocation cell structure. The second sample was fully recrystallized at 400 °C for 10 min. The third sample was left in the as-cold-rolled condition, where dislocations form entangled networks. Tensile tests were conducted on all three types of samples (Fig. 1).

The tensile specimens had 50 mm gauge lengths and 5 mm × 1 mm cross-sections. They were exposed to a uniaxial tensile load at an initial strain rate of $1.67 \times 10^{-5}\ s^{-1}$. Two methods were used for imaging the PLC bands. The first method is a laser speckle technique (LST) [36], which uses a laser beam to illuminate the sample surface, imaging local strains via changes in the speckle pattern. A high-speed camera (FASTCAM 1024PCI) captured

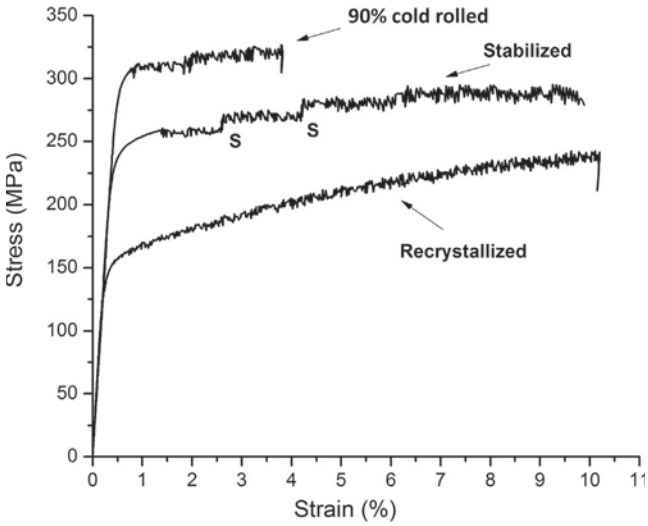

Fig. 1. Stress–strain curves of an Al-4.8 at.% Mg alloy (90% thickness reduction, cold rolled) in three conditions, i.e. recrystallized (400 °C, 10 min), stabilized (120 °C, 20 h) and as-cold rolled (reference state). Sudden stress shifts in the stabilized material are marked by S.

500 frames s^{-1} at a resolution of 128 × 512 pixels. The second method is imaging the bands in terms of temperature fields [37–39], where the dissipative deformation heat is mapped. The temperature variations range from a few hundredths to almost 0.5 °C. An infrared thermographic camera (VarioCAM HR inspect) with a sensitivity of 0.03 K and 50 frames s^{-1} at 640 × 480 pixels spatial resolution was chosen. Both methods were applied simultaneously during straining at room temperature (~23 °C).

The investigation of the Al–Mg alloy by APT was divided into two steps. The first one comprised the investigation of samples in the two heat-treated conditions. The second step consisted in probing regions directly inside the PLC bands. For this measurement, the tensile test was interrupted upon observation of a band. Site-specific atom probe and TEM specimens were then extracted from this PLC band by using a focused ion beam (FIB).

Atom probe samples from the stabilized condition were prepared by electropolishing [21]. For both the recrystallized state and the PLC band investigation, samples were prepared by a dual-beam FIB (FEI Helios NanoLab 600™). Site-specific sample preparation was conducted according to the lift-out protocol described in Ref. [40]. A 100 nm thick protective layer of platinum was deposited by FIB on the regions of interest (ROIs) before lift-out. FIB shaping of the specimens was performed at 30 kV ion beam voltage with a final milling step at 2 kV in order to control Ga implantation [40]. APT experiments were carried out using an Imago LEAP™ 3000X HR metrology system in voltage pulsed mode at 200 kHz repetition rate with a specimen temperature of about 30 K.

TEM investigations of the Al–Mg alloy were divided into two steps. The first set of experiments were carried out on a region inside a PLC band which had formed during a tensile test conducted on the recrystallized specimen. In a second set of experiments, we used the FIB-implanted Ga ions for decoration and, hence, identification of dislocation configurations. Since the Ga might affect defect configurations, we studied and compared dislocation structures before and after Ga implantation. This investigation was

done using undeformed recrystallized samples containing a low dislocation density. The TEM samples were inserted into the FIB for Ga ion-beam imaging. An ion-beam setting with 10 kV and 120 pA was used as a first step to image an area of 0.51 mm^2 in the center of the sample (~100 nm thickness) for 18 min. In the second step, 5 kV and 15 pA were applied to scan the beam across the same area for 6 min. These steps were chosen to reach the same average concentration of Ga in the TEM sample as detected in the atom probe measurements. A concentration of ~0.06 at.% Ga was calculated, using ion beam flux calculations such as explained in Ref. [41], to be implanted in the central region of the TEM sample during FIB exposure. Dislocations in the ROIs were compared before and after this Ga treatment.

For TEM analysis, foils were prepared as cross-sections through the cold-rolling direction. They were thinned to 150 μm, where the final thinning was achieved by electropolishing using a double-jet Tenupol apparatus and a 30% nitric acid/70% methanol solution at −31 °C and 35–160 mA for 2–3 min. The foils were investigated with a JEOL JEM-2200 FS™ microscope at 200 kV in scanning TEM (STEM) mode.

3. Results

3.1. Tensile testing

Stress–strain serrations were observed for all alloy conditions probed (Fig. 1). The onset of the serrations and the tensile strength differed among the specimens due to differences in dislocation density and microstructure. Larger stress jumps (marked S) were noticed for the stabilized condition in accord with earlier experimental studies on Al–Mg alloys [13,42]. The angle between the band front and the tensile axis amounted to 60–65°. The average velocity of the bands changed during straining within a range of 2.0–5.0 mm s^{-1}. The bulk temperature of the samples increased by 2–3 °C during each measurement, where each PLC band was associated with a local incremental temperature increase of 0.08–0.12 °C (the thermographic data are not shown here). The flow patterns observed fall into the *hopping type* PLC band category, referred to as type B bands [8], as observed before for this alloy type, strain rate and temperature. Subtracting two successive images from each other, each extracted from the recorded video of the LST measurements, reveals the PLC bands that are in good contrast (Fig. 2). The LST method turned out to be most efficient in locating the bands during measurements for enabling the subsequent site-specific FIB sample preparation. The tensile measurements were repeated several times and the samples were marked from the side using a millimeter scale bar. The markings were used for precisely defining the location of the last propagating band at the moment the tensile machine was stopped. The average bandwidth was about 2.0 mm. The macroscopic strain in the tensile sample used for site-specific preparation was $\varepsilon = 9.0\%$.

Fig. 2. Subtraction of two successive frame images obtained by LST revealing a PLC band in the middle of the tensile specimen; recrystallized sample state (50 mm gauge length).

3.2. APT measurements

The success rate of atom probe analyses of highly deformed samples is usually low due to the pulsed mechanical loading imposed during the measurements [43]. However, 3–5 million ions were collected from several samples containing solute-decorated dislocation substructures. The low alloying content enables clear crystallographic poles to be obtained in the APT data sets [29–31], from which the lattice spacing and respective angles were identified. The ion density map in Fig. 3 shows crystallographic poles in the stabilized specimen (120 °C, 20 h).

In the same data set, two Mg-decorated dislocations were detected. The dislocations were both aligned along the <1 1 0> crystallographic direction, with decoration concentrations of ~12.5 at.% Mg. Fig. 4a shows one of them. An isoconcentration surface is used to highlight the second dislocation segment (Fig. 4b). One should note that the dislocation vectors presented here are locally averaged alignment values, since most dislocations detected were not perfectly linear. A 1-D concentration profile was used to measure the Mg concentration across the second dislocation (Fig. 4c). The data in the rectangular ROI that was chosen to measure the profile was sampled at 1000 fixed ions per sampling block to minimize statistical errors.

Implanted Ga was detected in most atom probe samples prepared by FIB, with a bulk concentration range of 0.02–0.10 at.% (after background noise subtraction). The Ga decorates dislocations with concentrations of up to 1.80 at.% (Fig. 5). Mg was homogeneously distributed along the Ga-decorated dislocations in the recrystallized samples, but very inhomogeneously distributed inside the PLC bands. In APT samples taken from regions inside the PLC bands, the Mg formed depletion zones next to the dislocations on one side and showed slight segregation

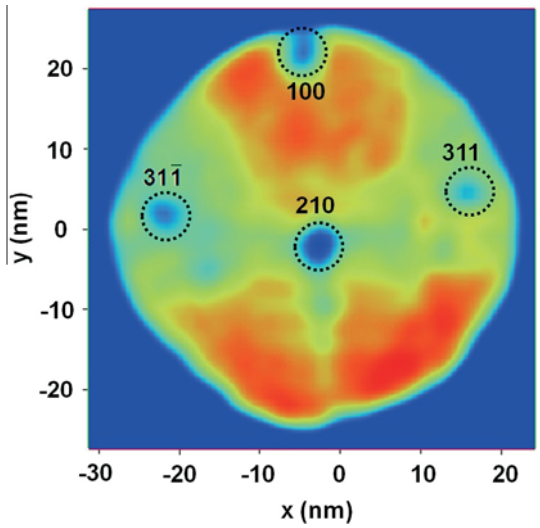

Fig. 3. *xy*-plane Al ion density map obtained for a sample in the stabilized condition (120 °C, 20 h) for a data slice of 30 nm thickness in the *z*-direction as measured by APT. The main poles have been identified to enable atom probe crystallographic analysis of the dislocation line alignment.

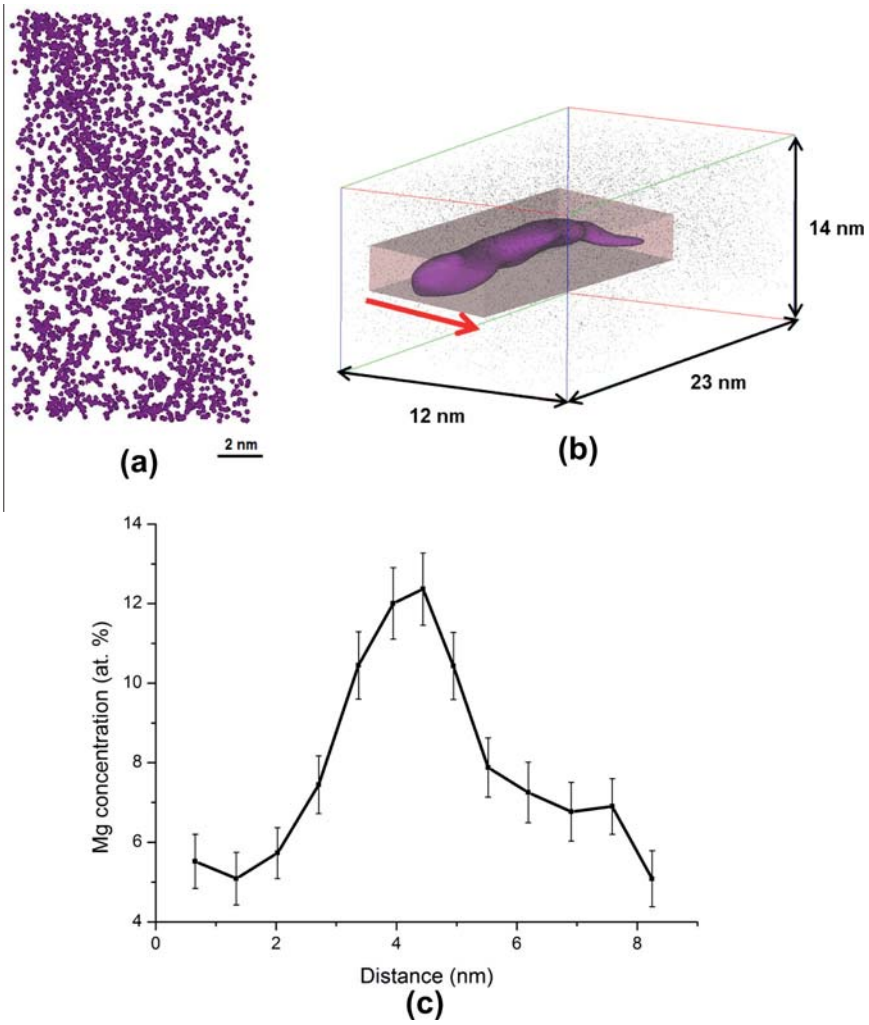

Fig. 4. (a) Sub-section (4 nm in depth) of a reconstruction showing an Mg-decorated dislocation along the <1 1 0> line direction in the stabilized specimen condition (120 °C, 20 h). (b) A second dislocation from the same sample with the same direction is highlighted using an isoconcentration surface. The rectangular parallelepiped placed around the dislocation shows the region chosen for 1-D concentration profile evaluation. The red arrow indicates the direction of the profile measurement. (c) A 1-D concentration profile across the Mg-decorated dislocation shown in (b) (Al ions not revealed). (For interpretation of the references to color in this figure legend, the reader is referred to the web version of this article.)

on the other side. Three APT data sets obtained from PLC bands revealed similar asymmetric distributions of Mg around the probed dislocation segments. The dislocations studied by APT from regions inside the PLC band had various crystallographic alignments. One of the data sets shown in Fig. 6a reveals two Ga-decorated dislocations, along the <1 1 4> and <1 1 0> directions, respectively. The reconstruction is slightly rotated (by 10°) about the main tip axis (Fig. 6b) to better visualize the planar depletion zones next to the two dislocations. The same tip also contains two grain boundaries (GBs), along the bottom of the volume probed, which are enriched in Ga and depleted in Mg. The regions containing the two dislocations are highlighted using Ga isosurfaces (Fig. 6c). Fig. 7a shows a segment of the <1 1 4> dislocation line, taking a perspective along the dislocation core. The data set enclosed a relatively large probed volume surrounding the <1 1 4> dislocation segment, enabling us to reveal both the solute content around the dislocation core and the extended tail-like solute interaction regime. A 2-D concentration map of Mg clearly shows the solute distribution surrounding the dislocation (Fig. 7b). The difference in Mg content observed between the regions above the glide plane and those below it was similar in all dislocation segments studied, namely, around 6 at.% Mg.

Regarding such high absolute levels in the Mg concentration variation around the dislocation lines, we expect no relevant experimental errors associated with the evaporation sequence, e.g. due to the evaporation field disparity between Al and Mg: the theoretically and experimentally observed field strengths values for Al and Mg are 19 and 21 V nm^{-1}, respectively [21]. Using field evaporation simulations, it was shown by Vurpillot et al. [44] that, for evaporation field discrepancies in a range within 1–10%, no substantial differences in the detected ion densities occur in the reconstruction as a result of the local magnification effect.

3.3. TEM investigations

TEM investigations conducted on a PLC band showed a very high dislocation density, with very few straight dislocation segments (Fig. 8a). Thus, no preferential orientations of the dislocations or slip bands were observed, as

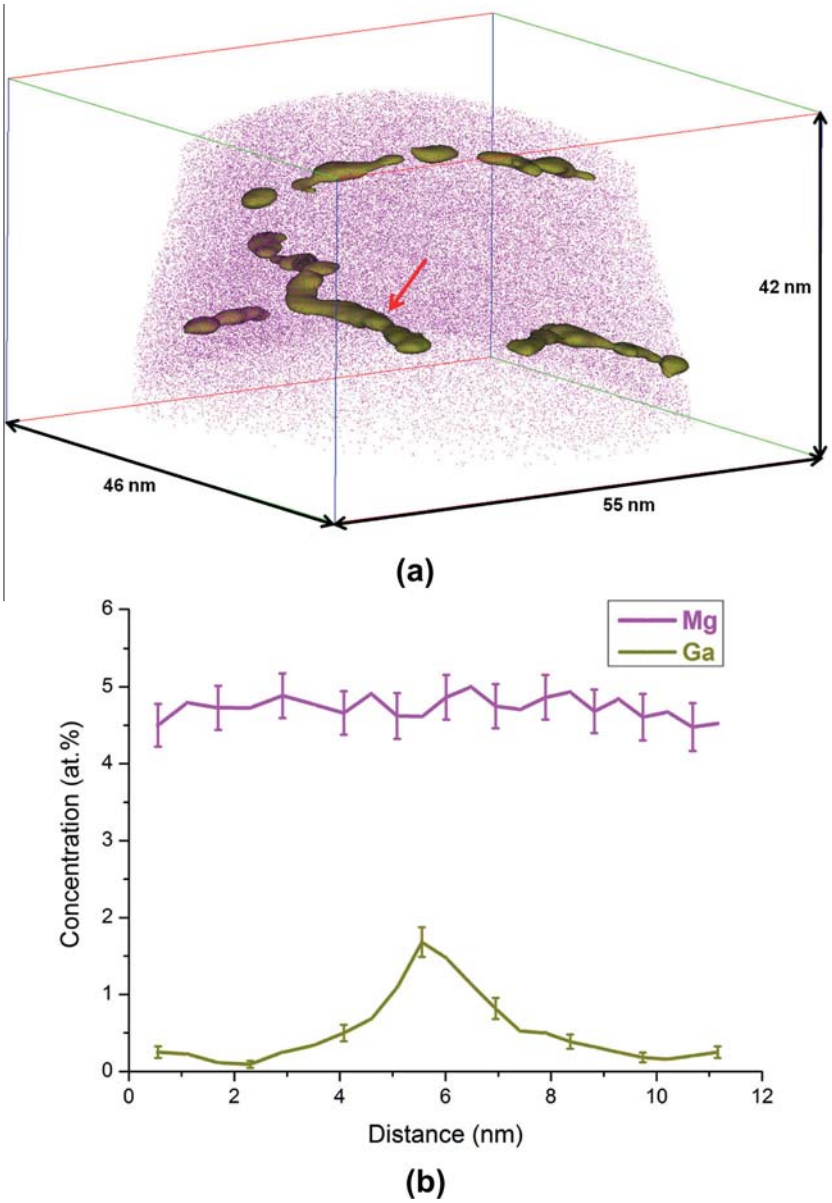

Fig. 5. (a) 3-D reconstruction of a sample in recrystallized condition prepared by FIB showing only Mg atoms. Isoconcentration surfaces for 1.5 at.% Ga revealing four linear segregation regions representing decorated dislocations after sample preparation. An ROI (not shown) was chosen on the marked dislocation for 1-D concentration profile analysis. (b) Mg concentration profile diagram along the marked dislocation (Al ions are not revealed).

was also reported in Ref. [45]. A higher dislocation density was usually found near GBs. The dense dislocation network explains the different dislocation line orientations observed in the crystallographic analysis of the different APT data sets. Ga diffusion into the sample does not affect the dislocation configurations, as can be observed by TEM. This is seen in Fig. 8b and c, which shows a few dislocations in a single grain from an undeformed recrystallized sample before and after the Ga treatment.

4. Discussion

One main point in the debate about the atomistic understanding of the DSA effect in Al–Mg alloys is how the solute Mg actually interacts with dislocations during deformation, since Mg atoms have a very low diffusion rate in Al, namely, only 10^{-9} nm^2 s^{-1} at room temperature [46]. McCormick's model [3], extended by Van Den Beukel [4], considered an increase in both vacancy concentration and dislocation density during straining to explain enhanced solute diffusion. Later, several models [5–10] excluded conventional bulk diffusion phenomena in conjunction with vacancy transport as an underlying reason and suggested instead that pipe diffusion of solute atoms along both mobile and forest dislocations is the main DSA-related transport mechanism. In contrast to this view, Curtin et al. [11] suggested the cross-core model, which introduces an alternative explanation for the high apparent solute mobility during straining of Al–Mg alloys. The model assumes that the Mg diffusion controlling DSA occurs inside the dislocation core, namely, from the compression

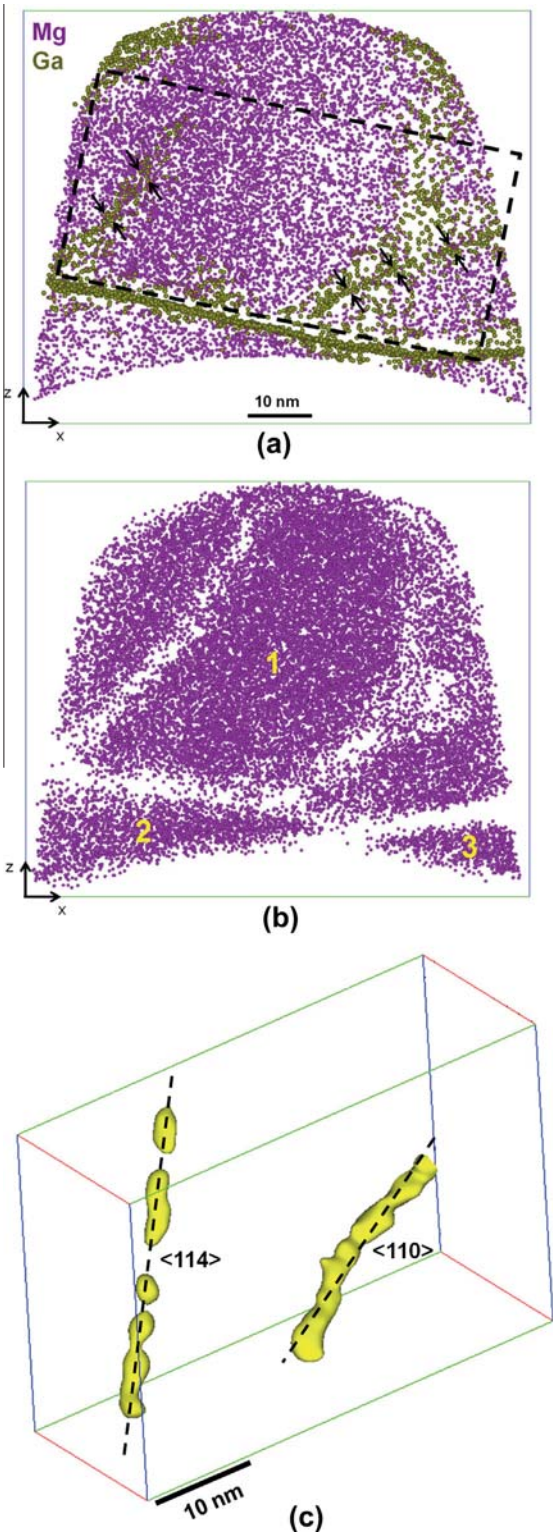

Fig. 6. A slice (20 nm thickness) taken from a reconstruction volume of a sample prepared from outside of the PLC band region ($\varepsilon = 0.09$). It shows two Ga-decorated dislocations and two grain boundaries (located at the bottom) decorated by Ga segregation. (a) The APT data set analysis reveals the positions of the Ga and Mg ions. The two dislocations are indicated by arrows. (b) The same region, rotated by 10° along the z-axis (30 nm thick slice), with only Mg depicted, revealing the Mg-depleted zones. The three grains in the sample are numbered 1–3. (c) Isoconcentration surface for 1.5 at.% Ga showing the two dislocations extracted from the dotted region marked in (a).

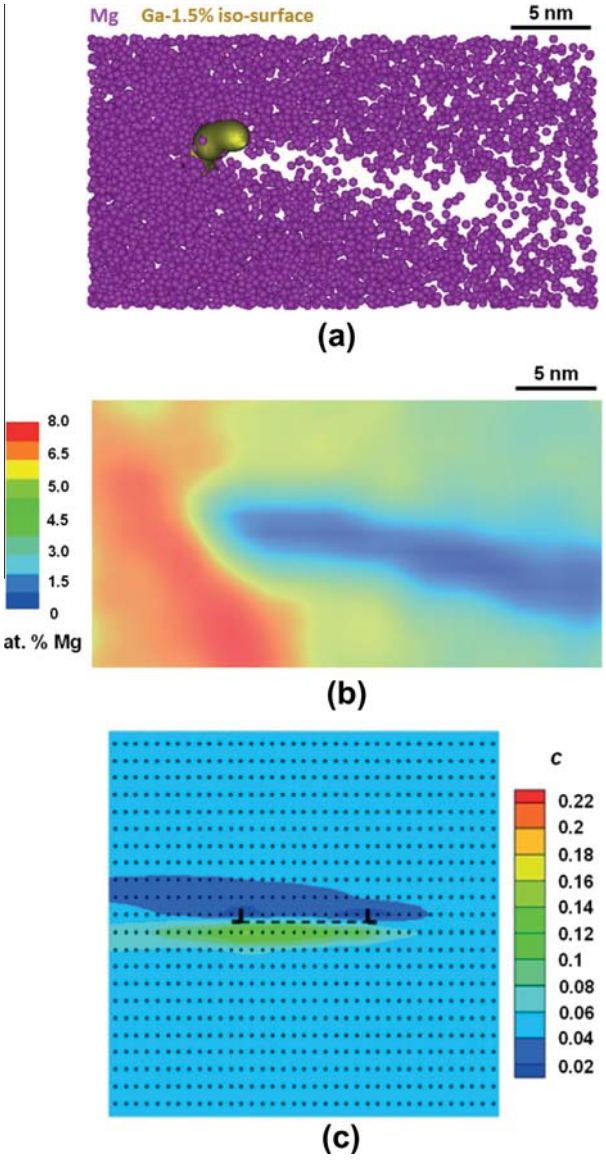

Fig. 7. Slice from the APT data set reconstruction (12 nm thickness) containing a dislocation segment, taking a perspective along the <1 1 4> line direction (full dislocation is shown in Fig. 6). This view provides a perspective of the inhomogeneous Mg distribution across the dislocation core and also the long depletion tail behind it. (a) The dislocation core is highlighted in terms of a 1.5 at.% Ga isoconcentration surface. (b) 2-D concentration map showing the Mg distribution on both sides of the dislocation. (c) Image of the solute drag simulation of Zhang and Curtin [18], revealing the asymmetry of the solute distribution around a moving dislocation at velocities above the peak drag stress (c represents the atomic concentration of Mg).

side to the tension side of the dislocation slip plane. The approach predicts very high solute concentrations on the tension side and very low concentrations on the compression side of a dislocation slip plane, respectively (Fig. 7c). The model shows very good agreement with experimental DSA stress–strain data over a wide range of concentrations and temperatures. The present work provides for the first time experimental atomic-scale proof for the arrangement of the Mg atoms around a dislocation as assumed in Curtin's model (Fig. 7a and b).

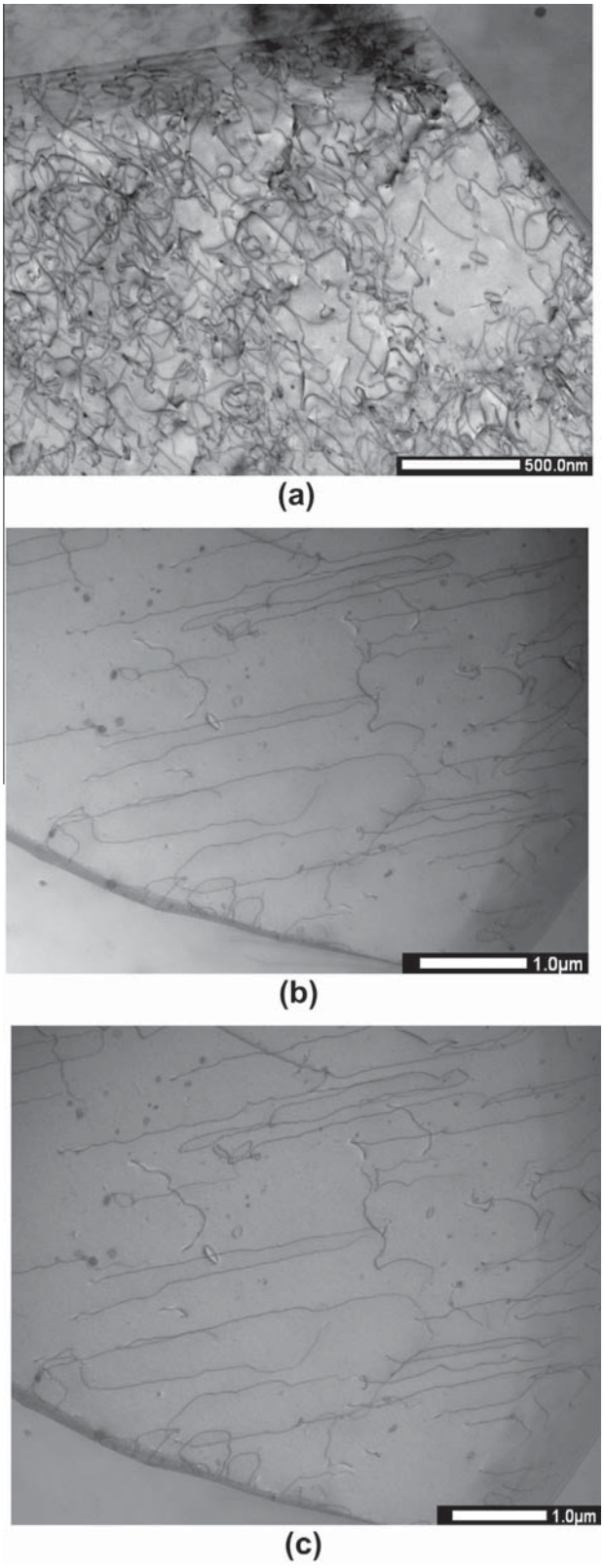

Fig. 8. Bright-field STEM images of the Al–Mg alloy. (a) High dislocation density in a sample prepared from a region inside of a PLC band ($\varepsilon = 0.09$) from the tensile specimen (recrystallized condition). A grain with low dislocation density from an undeformed sample (b) before Ga treatment and (c) after Ga treatment.

To understand the dynamics of SADI and its influence on the PLC effect, the solute drag on moving dislocations during straining has to be taken into account. Zhang and Curtin [18] introduced a model that describes solute drag on a moving dislocation in a deforming Al–Mg alloy, taking the cross-core diffusion mechanism into consideration. They used it to study the magnitude of the solute drag effect as a function of the dislocation velocity, as well as the role of lattice diffusion vs. cross-core diffusion at different dislocation speeds, respectively. The present experimental results, observed directly inside a PLC band, show full agreement with the model predictions of Zhang and Curtin [18] for the case of high dislocation velocities (Fig. 7).

The simulations reveal that, at dislocation velocities above a critical value, v_c, corresponding to the peak drag stress, the Mg concentration drastically depletes in the compressive regime above the dislocation slip plane and increases below the slip plane in the dilatation region. This leads to a very asymmetric Mg distribution around the dislocation core. At even higher dislocation velocities, the drag stress decreases and the solute cloud cannot contribute substantially to the drag stress. The simulations show that, in this case, the Mg depletion assumes a tail-like narrow shape that forms behind the moving defect. An image of the simulation results is shown in Fig. 7c, indicating an excellent agreement with the present experimental observations (Fig 7a and b).

Another simulation approach on solute drag by Hu et al. [17], based on a phase-field method that is independent of specific material constants, also reproduces some of the current experimental findings. Although not including the cross-core mechanism, Hu et al. considered chemical and elastic interactions among solutes and dislocations, offering a more realistic approach compared to earlier solute drag models [14,15]. They simulated the effects of varying solute compositions, applied stresses and different solute-to-dislocation mobility ratios on the resulting solute–dislocation dynamics. Interestingly, for the case of a solute-to-dislocation mobility ratio approaching zero, i.e. assuming negligible Mg bulk lattice diffusion in Al alloys, their model predicts a higher average dislocation velocity and the formation of tail-like solute atmospheres surrounding the dislocation cores. Except for the fact that this model does not consider realistic materials constants and does also not consider the low-barrier and low-range cross-core diffusion mechanism introduced by Curtin et al. [11], a similar tail-shaped Mg depletion trend as observed in our present experiments is predicted.

Hu et al. [17] also suggested the occurrence of a periodic variation in the dislocation velocity and dragging stress during dislocation motion. They suggested that this phenomenon be linked to the temperature and strain rate dependence of the serrations in the stress–strain curves, i.e. the PLC effect, since the mobility of the substitutional elements depends on temperature.

Since the APT measurements presented here were carried out in regions inside a PLC band, we interpret the results in terms of the high-velocity dislocation regime, above v_c, in agreement with the solute drag models used here for comparison [17,18].

The fact that we observe relatively large depletion tail zones, namely, ~30 nm (lateral direction), strongly suggests

that these slip plane regions represent highly favorable zones for the movements of other dislocations. This means that the reorganization (depletion) of Mg atoms behind a fast moving dislocation promotes the glide of further dislocations along the same, but softened, glide path. This effect leads to a nonlinearity explaining the strong self-maintaining softening effect (points marked by S in Fig. 1) in a local peak stress scenario where a dislocation breaks away and reaches its maximum velocity. Although this mechanism alone leads to softening, the fact that other dislocations follow the same path at a lower glide resistance should enhance the phenomenon. This means that further slip is greatly facilitated behind fast-moving dislocations, promoting slip localization and the formation of dislocation avalanches. Indeed, recent works by Hong and Lee [47] and Nikulin and Kaibyshev [48] have revealed such planar slip features in the DSA regime of stainless steels, leading to a well-defined band structure [49,50].

The different results obtained for the Mg distribution around the dislocations in the stabilized and recrystallized conditions, respectively, can be explained as follows. For the stabilized condition, cold rolling in conjunction with a modest decoration heat treatment (120 °C, 20 h) has enabled lattice diffusion of Mg and segregation to dislocations, i.e. the formation of Cottrell clouds [2]. The segregation values observed here fit kinetic Monte Carlo simulations by Xu and Pico [51] for the case of Al-5.0 at.% Mg. Dislocations detected in the recrystallized condition, i.e. without Mg segregation, suggest that Mg solute atoms interact with dislocations when loaded into the DSA regime, due to the cross-core diffusion mechanism acting on mobile dislocations, as discussed by Curtin et al. [11], or segregate to immobile dislocations at higher temperatures due to lattice diffusion.

5. Conclusions

We studied dynamic strain aging in an Al-4.8 at.% Mg alloy at the atomic scale by APT and TEM. APT tips were extracted from regions inside PLC bands. We draw the following conclusions:

- Ga introduced by FIB preparation decorates dislocations in the alloy, assisting in identifying them in the APT data sets without influencing their configurations.
- Quasi-static Mg decoration to sessile <1 1 0> aligned dislocations outside of the PLC bands amounts to ~12.5 at.%, in accord with the kinetic Monte Carlo simulations of Xu and Picu [51].
- Inside the PLC bands, fast dislocations breaking free at peak drag stress lead to an asymmetric Mg distribution, characterized by depletion in the compressive zone above the slip plane to values below 0.5 at.% and enrichment in the dilatation zone below the slip plane to values up to around 8 at.%, which matches the solute-drag simulations of Zhang and Curtin [18].
- The enrichment (±1 at.% deviation) and depletion (±0.2 at.% deviation) of Mg, respectively, around the dislocation match the cross-core DSA predictions of the model of Curtin et al. [11].
- Behind fast dislocations, a large tail-like zone was depleted of Mg, extending to about 30 nm. We suggest that such Mg-depleted zones cause local softening, hence promoting slip localization and enhancing negative strain rate sensitivity as well as planar slip. This phenomenon could explain the collective motion of a larger number of dislocations, leading to macroscopically visible stress–strain serrations.

References

[1] J.E. Hatch, Aluminium: Properties and Physical Metallurgy, ASM International, Materials Park, OH, 1984.
[2] A.H. Cottrell, B.A. Bilby, Proc. Phys. Soc. A 62 (1948) 49–62.
[3] P.G. McCormick, Acta Metall. 20 (1972) 351–354.
[4] A. Van Den Beukel, Phys. Stat. Sol. (a) 30 (1975) 197–206.
[5] R.A. Mulford, U.F. Kocks, Acta Metall. 27 (1979) 1125–1134.
[6] L.P. Kubin, Y. Estrin, Acta Metall. Mater. 38 (1990) 679–708.
[7] L.P. Kubin, Y. Estrin, Phys. Stat. Sol. (b) 172 (1992) 173–185.
[8] S. Kok, M.S. Bharathi, A.J. Beaudoin, C. Fressengeas, G. Ananthakrishna, L.P. Kubin, M. Lebyodkin, Acta Mater. 51 (2003) 3651–3662.
[9] R.C. Picu, Acta Mater. 52 (2004) 3447–3458.
[10] C. Fressengeas, A.J. Beaudoin, M. Lebyodkin, L.P. Kubin, Y. Estrin, Mat. Sci. Eng. A 400 (2005) 226–230.
[11] W.A. Curtin, D.L. Olmsted, L.G. Hector, Nat. Mater. 5 (2006) 875–880.
[12] G.P.M. Leyson, L.G. Hector Jr., W.A. Curtin, Acta Mater. 60 (2012) 3873–3884.
[13] R.C. Picu, G. Vencze, F. Ozturk, J.J. Gracio, F. Barlat, A.M. Maniatty, Mater. Sci. Eng. A 390 (2005) 334–343.
[14] A.H. Cottrell, M.A. Jaswon, Proc. R. Soc. Lond. A 199 (1949) 104–114.
[15] H. Yoshinaga, S. Morozumi, Philos. Mag. 23 (1971) 1367–1385.
[16] J.P. Hirth, J. Lothe, Theory of Dislocations, 2nd ed., Wiley, New York, 1982.
[17] S.Y. Hu, J. Choi, Y.L. Li, L.Q. Chen, J. Appl. Phys. 96 (2004) 229–236.
[18] F. Zhang, W.A. Curtin, Model. Simul., Mater. Sci. 16 (2008) 1–18.
[19] T.F. Kelly, T.T. Gribb, J.D. Olson, R.L. Martens, J.D. Shepard, S.A. Wiener, T.C. Kunicki, R.M. Ulfig, D.R. Lenz, E.M. Strennen, E. Oltman, J.H. Bunton, D.R. Strait, Microsc. Microanal. 10 (2004) 373–383.
[20] T.F. Kelly, B.P. Geiser, D.J. Larson, Microsc. Microanal. 13 (2007) 1604–1605.
[21] M. Miller, Atom Probe Tomography, Kluwer Academic/Plenum Press, New York, 2000.
[22] F. Vurpillot, G. Da Costa, A. Menand, D. Blavette, J. Microsc. 203 (2001) 295–302.
[23] B.P. Geiser, T.F. Kelly, D.J. Larson, J. Schneir, J.P. Roberts, Microsc. Microanal. 13 (2007) 437–447.
[24] T. Boll, T. Al-Kassab, Y. Yuan, Z.G. Liu, Ultramicroscopy 107 (2007) 796–801.
[25] M.P. Moody, B. Gault, L.T. Stephenson, D. Haley, S.P. Ringer, Ultramicroscopy 109 (2009) 815–824.
[26] M.K. Miller, J. Mater. Sci. 41 (2006) 7808–7813.
[27] D. Blavette, E. Cadel, A. Fraczkiewica, A. Menand, Science 286 (1999) 2317–2319.
[28] M.J. Duarte, J. Klemm, S.O. Klemm, K.J.J. Mayrhofer, M. Stratmann, S. Borodin, A.H. Romero, M. Madinehei, D. Crespo, J. Serrano, S.S.A. Gerstl, P.P. Choi, D. Raabe, F.U. Renner, Science 341 (2013) 372–376.
[29] V.J. Araullo-Peters, B. Gault, S.L. Shrestha, L. Yao, M.P. Moody, S.P. Ringer, J.M. Cairney, Scripta Mater. 66 (2012) 907–910.
[30] P.V. Liddicoat, X. Liao, Y. Zhao, Y. Zhu, M.Y. Murashkin, E.J. Lavernia, R.Z. Valiev, S.P. Ringer, Nat. Commun. 1 (2010) 1–7.
[31] B. Gault, M.P. Moody, J.M. Cairney, S.P. Ringer, Mater. Today 15 (2012) 378–386.

[32] M. Herbig, D. Raabe, Y.J. Li, P. Choi, S. Zaefferer, S. Goto, Phys. Rev. Lett. 112 (2014) 126103.
[33] W. Guo, E.A. Jägle, P.-P. Choi, J. Yao, A. Kostka, J.M. Schneider, D. Raabe, Phys. Rev. Lett. 113 (2014) 035501.
[34] Y.J. Li, D. Raabe, M. Herbig, P.-P. Choi, S. Goto, A. Kostka, H. Yarita, C. Borchers, R. Kirchheim, Phys. Rev. Lett. 113 (2014) 106104.
[35] Y.J. Li, P. Choi, C. Borchers, S. Westerkamp, S. Goto, D. Raabe, R. Kirchheim, Acta Mater. 59 (2011) 3965–3977.
[36] R. Shabadi, S. Kumar, H.J. Roven, E.S. Dwarakadasa, Mater. Sci. Eng. A364 (2004) 140–150.
[37] H. Ait-Amokhtar, C. Fressengeas, S. Boudrahem, Mater. Sci. Eng. A448 (2008) 540–546.
[38] H. Louche, P. Vacher, R. Arrieux, Mater. Sci. Eng. A 404 (2005) 188–196.
[39] A. Eisenlohr, I. Gutierrez-Urrutia, D. Raabe, Acta Mater. 60 (2012) 3994–4004.
[40] D. Lawrence, K. Thompson, D. Larson, B. Gorman, Microsc. Microanal. 12 (2006) 1742–1743.
[41] I. Utke, P. Hoffmann, J. Melngailis, J. Vac. Sci. Technol. B 26 (2008) 1197–1276.
[42] K. Chihab, Y. Estrin, L.P. Kubin, J. Vergnol, Scripta Metall. 21 (1987) 203–208.
[43] M.K. Miller, A. Cerezo, M.G. Hetherington, G.D.W. Smith, Atom Probe Field Ion Microscopy, Oxford University Press, Oxford, 1996.
[44] F. Vurpillot, A. Bostel, D. Blavette, Appl. Phys. Lett. 76 (2000) 3127.
[45] D. Park, M. Niewczas, Mater. Sci. Eng. A 491 (2008) 88–102.
[46] Y. Du, Y.A. Chang, B. Huang, W. Gong, Z. Jin, H. Xu, Z. Yuan, Y. Liu, Y. He, F.-Y. Xie, Mater. Sci. Eng. A363 (2003) 140–151.
[47] S. Hong, S. Lee, J. Nucl. Mater. 340 (2005) 307–314.
[48] I. Nikulin, R. Kaibyshev, Mater. Sci. Eng. A 528 (2011) 1340–1347.
[49] V. Gerold, H.P. Karnthaler, Acta Metall. 37 (1989) 2177–2183.
[50] H. Neuhäuser, O.B. Arkan, H.-H. Potthoff, Mater. Sci. Eng. 81 (1986) 201–209.
[51] Z. Xu, R.C. Picu, Model. Simul. Mater. Sci. Eng. 14 (2006) 195–206.